Journal of Computational Physics **166,** 336–360 (2001)
doi:10.1006/jcph.2000.6658, available online at http://www.idealibrary.com on IDEAL®

3D Jet Impact and Toroidal Bubbles

Y. L. Zhang,* K. S. Yeo,† B. C. Khoo,* C. Wang*

*Institute of High Performance Computing, 89-B Science of Park Drive, No. 01-05/08 The Rutherford, Singapore Science Park I, Singapore 118261; and †Department of Mechanical and Production Engineering, National University of Singapore, Kent Ridge, Singapore 119260, Republic of Singapore
E-mail: hpczyl@nus.edu.sg, mpeyeoks@nus.edu.sg, kbc@ihpc.nus.edu.sg

Received October 2, 1999; revised August 29, 2000

A three-dimensional model of collapsing bubble with jet formation and impact is presented in this paper. The strong instabilities of the jetting process, impact, and toroidal bubble rebound are dampened by a new smoothing scheme based on least squares, thus enabling a smooth transition from a singly connected bubble to a doubly connected toroidal bubble. A high order of mesh regularity is maintained by a mesh refinement procedure. The circulation of the flow around the gaseous tube of the toroidal bubble is modelled by a generalization of the vortex ring method of Q. X. Wang *et al.* (*Comput. Fluids* **25**, 607 (1996)). Although our results indicate some differences from previous axisymmetric results in terms of time to impact and fine features of the evolving toroidal bubble profiles, the essential physics associated with the jet impact, such as the circulation around the torus and the rebound of the toroidal bubble, are well captured in the new model. We also present, for the first time, results for fully three-dimensional bubbles in which buoyancy effects lead to oblique jetting.

Key Words: 3D toroidal bubbles; 3D jet impact; boundary integral equations.

1. INTRODUCTION

During the collapse of an initially spherical bubble near a rigid wall, different parts of the bubble contract at drastically different rates: the part farthest from the wall moves the fastest, and the part nearest to the wall the slowest because of the constraining influence of the wall. This imbalance results in the surface of the bubble on the far side deforming into a liquid jet directed at the wall. Fluid on the far side of the bubble rushes into this developing jet, which advances to hit the opposite face of the bubble. The impact transforms the originally simply connected bubble into a bubble of toroidal form and imparts a circulation to the flow around the gaseous tube of the toroidal bubble. In engineering practice, the high-speed jet is often associated with the damage caused by collapsing cavitation bubbles to hydraulic machinery. The high-speed jets produced by large collapsing bubbles are also known to

0021-9991/01 $35.00

inflict devastating damages on submerged surfaces and vessels. Excellent reviews on this subject may be found in Plesset and Prosperetti [1], Blake and Gibson [2], and Blake *et al.* [3].

Previous theoretical studies on bubble dynamics have tended to focus on cases of spherical and axisymmetric bubbles. Much about the phenomenon of bubble jetting has been understood through these studies (Guerri *et al.* [4]; Blake *et al.* [5]). In particular, it was found that the main damage is done to the structure during the toroidal phase, i.e., after the jet impact [5, 6]. The formation of toroidal bubbles from the jetting of axisymmetric bubbles was first computationally simulated by Best [7, 8]. He continued the computation into the toroidal phase with the aid of a *cut surface* that represents the impact surface. The domain cut was introduced to render a nominally singly connected domain. A similar domain-cut procedure was used by Zhang *et al.* [9], whose model also allows a shear layer to be generated along the cut surface during the impact. Recently, Wang *et al.* [6], utilizing a concept due to Lundgren and Mansour [10], proposed that the flow circulation generated during jet impact be modelled by a vortex ring placed *inside* the tube of the toroidal bubble. This ingenious device removes the discontinuity of the velocity potential due to non-zero flow circulation, and hence also the need for an explicit domain cut.

It is only recently that researchers have begun to explore the simulation of three-dimensional (3D) bubbles [11–15]. Zhang *et al.* [14] introduced a trivariate representation of surface elements in the form of the 9-noded Lagrangian element and applied the model to multiple bubbles in the presence of a free surface. The trivariate element provides a consistent representation of the bubble surface in a single global coordinate frame, whereas the more customary bivariate representations require the use of local frames. Zhang *et al.* [15] explored the application of a desingularized indirect boundary-integral procedure to the simulation of 3D bubbles. The desingularized indirect method represents the potential function as the arithmetic sum of the potentials of point singularities that are located inside the bubble (a short distance below the surface) rather than on the surface of the bubble as is customary with direct integral representations. It provides an element-free representation of the surface potential and was found to be highly efficient numerically. Despite the very different principles involved, the results of the 9-noded Lagrangian-element direct model and the desingularized indirect boundary integral formulation agree remarkably well with each other. These models fall short, however, when applied to cases that involve jet impact. Surgery has to be performed on the bubble surface during jet impact to create a toroidal bubble. The limitation of the 9-noded Lagrangian element is that each node can have at most 8 nodal neighbours. With mesh refinement, which is deemed to be essential to maintain element regularity for highly distorted bubbles, it is possible to end up with nodes having more than 8 neighbouring nodes. This is especially so during the surgical reconstruction of the bubble. The limitation of the desingularized formulation lies in the interior seeding of its singularities, which makes it difficult for opposing bubble surfaces to be brought into contact. The approach of the liquid jet is thus halted even earlier than for direct methods. To allow the jet to approach closer to the facing bubble surface, one may have to switch back at the appropriate point to a direct formulation. The above models are therefore not well suited to dealing with jet impact. The development of a 3D model that takes the evolution of the bubble through jet impact and beyond presents a significant challenge, which is the subject of the present paper.

The development of the high-velocity jet, the impact and formation of the toroidal bubble, and the follow-on evolution of the toroidal bubble together present a formidable problem, not the least because the transition to the new geometry is afflicted by strong instability. A 3D

model of collapsing bubbles with jet impact which incorporates features that are absent in the earlier models is described in this paper. The new model uses the same basic triangulation of the bubble surface. The initial mesh on the bubble tends to become highly distorted and stretched as the jet extends deep into the bubble. The resultant mesh irregularities spell trouble for numerical accuracy and conditioning. The regularity of the triangular mesh is maintained in the present model by a mesh refinement procedure that limits the size variation of elements around a nodal point. It can also limit the variation of element size over the whole bubble so that errors produced by the surgical reconstruction of the bubble to render a toroidal geometry are kept at a reasonable level. Strong instability is encountered as the jet approaches the opposite bubble surface. This and other instabilities that accompany the transition to toroidal geometry are kept in check by a local least-squares smoothing scheme. The smoothing procedure, which removes the noise generated by the instabilities, allows a reasonable time step to be used to carry forward the computation. The vortex ring method introduced by Wang *et al.* [6] to represent flow circulation for axisymmetric toroidal bubbles is extended to 3D bubbles here. In this approach, the potential of the flow is decomposed into a vortex-induced part and a remainder that is continuous throughout the fluid domain. The more complex geometry of the 3D bubble necessitates the use of non-planar ring.

The present model is found to be able to reproduce the essential physics of bubble jetting, flow circulation around the toroidal tube and the rebound of the toroidal bubbles. Some differences exist, however, between the present results and the axisymmetric results of Best [7, 8] and Wang *et al.* [6]; in the time to impact and fine features of the evolving toroidal bubbles. These differences are probably due to the more limited spatial resolution of the 3D cases. The overall agreement between the two models is nevertheless satisfactory. The new model is applied to collapsing 3D gas bubbles with non-negligible buoyancy. Buoyancy effects typically become significant when a bubble becomes large. Oblique jetting and the attendant impact are caused by a combination of buoyancy and Bjerknes effect due to the presence of a nearby wall.

2. AN IMPROVED 3D BUBBLE DYNAMICS MODEL

2.1. *A Weighted-Average Scheme*

Figure 1 shows a schematic view of the problem to be considered in this paper. We only look at the case of a pressure-driven gas bubble initiated near a rigid infinite wall in an incompressible fluid. Surface tension effects are not accounted for in this study because of the generally large size of the gas bubbles we have in mind. Viscous effects are also neglected because the timescale for viscous diffusion is much larger than the oscillation period for these bubbles. In addition, a rectangular coordinate system O-xyz is adopted with the origin located at the center of the initially spherical bubble and the z axis pointing in the opposite direction ot gravity (Fig. 1). The boundary of the bubble is denoted as S_b, which is a regular surface before and after the jet impact. The fluid domain is denoted by Ω and it is transformed from a singly connected to a doubly connected region during jet impact.

The pressure inside the bubble consists of two parts: a constant pressure of vapour p_c and the pressure of noncondensable gas that conforms to the adiabatic law,

$$p = p_c + p_0\left(\frac{V_0}{V}\right)^{\lambda}, \tag{1}$$

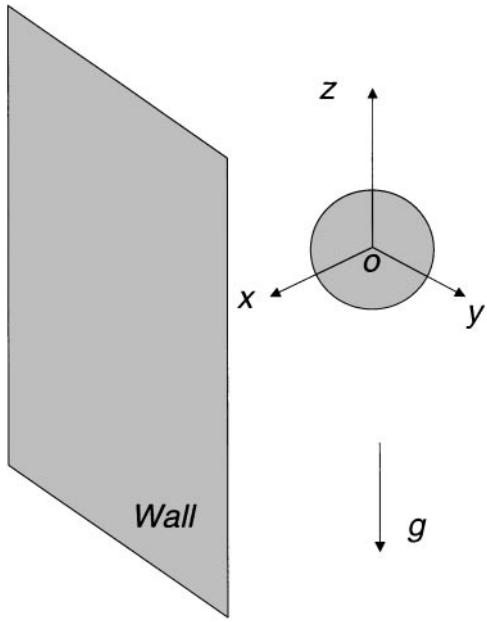

FIG. 1. A schematic view of the problem and the coordinate system used.

where V_0 and p_0 are the initial volume and pressure of the noncondensable gas, respectively, and λ is the ratio of specific heat of the gas. In this investigation we take $\lambda = 1.4$.

We then proceed to nondimensionalize the variables: with the length scale chosen to be the maximum bubble radius R_m, the pressure scale being $\Delta p = p_\infty - p_c$, where p_∞ is the ambient pressure at $z = 0$, and the density scale being ρ, the density of the liquid. R_m is the maximum radius that the bubble would attain in an unbounded fluid domain (the Rayleigh bubble) at the constant pressure of p_∞. The nondimensional parameters that characterize the problem are

$$\delta = \sqrt{\frac{\rho g R_m}{\Delta p}}, \quad \text{and} \quad \epsilon = \frac{p_0}{\Delta p}, \tag{2}$$

which measure the *buoyancy* effects and the *strength* of the initial pressure inside the bubble, respectively. In this paper, the parameters δ and ϵ are prescribed.

The potential theory dictates that there exists a velocity potential $\phi(x, y, z, t)$ which satisfies the well-known boundary integral equation

$$c(P)\phi(P) + \int_{S_b} \left[\phi(Q)\frac{\partial G(P, Q)}{\partial n(Q)} - G(P, Q)\frac{\partial \phi(Q)}{\partial n(Q)}\right] dS(Q) = 0, \tag{3}$$

where $c(P)$ is a geometrical constant depending only on the location of the field point P and $\mathbf{n}$ is the unit *outward* normal on the boundary. Note that the integral is carried out only on the bubble surface as the effect of the rigid wall has been taken into account in the Green function $G(P, Q)$

$$G(P, Q) = \frac{1}{|p - Q|} + \frac{1}{|\mathrm{P}' - Q|}, \tag{4}$$

with P' being the reflected image of P with respect to the wall. It is trivial to verify from (4) that $\frac{\partial G(P,Q)}{\partial n(Q)} = 0$ on the rigid wall.

The bubble deforms with time according to the following kinematic and dynamic boundary conditions,

$$\left.\begin{aligned} \frac{D\mathbf{x}}{Dt} &= \nabla\phi, \\ \frac{D\phi}{Dt} &= 1 + \frac{1}{2}|\nabla\phi|^2 - \delta^2 z - \epsilon\left(\frac{V_0}{V}\right)^{\lambda}, \end{aligned}\right\} \text{for } \mathbf{x} \in S_b, \tag{5}$$

where $\mathbf{x}$ is the position vector and $\frac{D}{Dt}$ denotes the material time derivative. From these equations it can be seen that it is essential to have an accurate scheme to evaluate the velocity $\mathbf{u} = \nabla\phi$ on the surface of the bubble. This has been a major issue in the boundary integral modeling of 3D bubbles [14, 16]. The flow velocity $\mathbf{u} = \nabla\phi$ generated by the bubble should tend to zero in the far field. This condition is automatically met by the choice of Green's function in (4).

The bubble is assumed to begin its existence at time $t = 0$ as a high-pressure spherical bubble of radius R_0 with zero wall velocity. The evolution of the bubble in the absence of buoyancy effects and far from any surfaces is governed by the Rayleigh equation

$$R\ddot{R} + \frac{3}{2}\dot{R}^2 = \epsilon\left(\frac{R_0}{R}\right)^{3\lambda} - 1. \tag{6}$$

With ϵ given, the initial radius R_0 may be solved by the reverse time integration of (6) from the nondimensional maximum radius of 1.0 to the radius R_0; following Best [7]. R_0 may alternatively be obtained by considering the conservation of potential energy between the initial state and the state of maximum radius, $R = 1$. The position of the rigid wall relative to the spherical initial bubble is also prescribed to complete the geometrical specification of the problem. Given the quiescent initial state, $\phi = 0$ throughout the entire fluid domain at $t = 0$.

The following discussions closely follow those in our recent paper [14]. The surface of the bubble is discretized into a series of linear triangular elements. The time marching is done using a second-order Runge–Kutta scheme. To maintain numerical stability, the time-step size δt is choson in accordance with the criterion

$$\delta t = \frac{\Delta\phi}{\max|D\phi/Dt|}, \tag{7}$$

which seeks to approximately limit the maximum change in the nodal potential at each time step to a specified constant $\Delta\phi$; the maximum in the denominator of (7) is taken over all the nodal points on the bubble with $D\phi/Dt$ given by (5). A value of 0.03 is set for $\Delta\phi$ in the computation. But an important distinction from [14] is the way the material velocity $\mathbf{u} = \nabla\phi$ is calculated. In anticipation of the need for an adaptive mesh as well as the complicated surgery to be performed during the jet impact, it is essential to have a simple, accurate algorithm for the calculation of velocity. The 9-noded Lagrangian element method in [14] proves to be cumbersome in this aspect and hence we adopt here a weighted-average scheme. This scheme is based on a simple idea that although the normals are undefined at the vertices of the polyhedron (the discretized bubble surface), it is well defined within on each triangular surface element. Therefore, after the normal velocity $\frac{\partial\phi}{\partial n}$ has been found from the boundary integral equation (3), we can obtain, using a finite difference scheme, the velocities along two tangential directions l and m (i.e., along two sides of the triangular

element). With this information, we can compute the velocity vector within each element supporting a particular vertex or node by solving the 3×3 matrix equation

$$\begin{pmatrix} n_x & n_y & n_z \\ l_x & l_y & l_z \\ m_x & m_y & m_z \end{pmatrix} \begin{pmatrix} u_i \\ v_i \\ w_i \end{pmatrix} = \begin{pmatrix} \frac{\partial \phi}{\partial n} \\ \frac{\partial \phi}{\partial l} \\ \frac{\partial \phi}{\partial m} \end{pmatrix}, \tag{8}$$

where $(u_i,\ v_i,\ w_i)$ is the velocity vector due to the ith element. Note that this matrix equation always has a solution because $\mathbf{n} = \mathbf{1} \times \mathbf{m} \neq \mathbf{0}$. Finally, the velocity at this vertex or node is obtained as the weighted average of all the $\mathbf{u}_i = (u_i,\ v_i,\ w_i)$, i.e.,

$$\mathbf{u} = \frac{\sum_i \frac{\mathbf{u}_i}{\Delta_i}}{\sum_i \frac{1}{\Delta_i}}, \tag{9}$$

where Δ_i stands for the area of the ith element surrounding the node. The weighting function Δ_i^{-1} is chosen so that a smaller element yields a bigger contribution to the average velocity than a larger element; we note that in calculus, a smaller element (increment) yields a more accurate approximation of the local properties than a larger one.

This new algorithm of computing the velocity, different from the ones employed by Wilkerson [11] and Harris [17], ensures the convergence of the solution. In their linear averaging scheme, the normal at a particualr node is approximated by averaging the normals of its surrounding elements. This has led to poor approximation of local properties, and even to nonconvergence of solution as the mesh is refined [16]. This may be easily understood, given that the accuracy of the computed normal is highly dependent on the regularity of its surrounding elements [16]. After all, the "true" normal at a vertex of a polyhedron is undefined. Our method, on the other hand, circumvents this dilemma by doing away with the use of the normal in velocity computation. As the mesh is refined, the computed velocity $\mathbf{u}_i$ in each element unexceptionally approaches the exact velocity and thus convergence is guaranteed.

The verify this, we apply the new method to a simple Rayleigh bubble which undergoes periodic expansion and contraction radially in an unbounded fluid. Despite the nonuniformity of elements surrounding a nodal point, the computed velocity converges to the radially directed velocity distribution of the Rayleigh bubble as the mesh is refined. The period of oscillation and maximum radius of the computed bubble also accurately match those of the Rayleigh bubble, as may be seen in Fig. 2, in stark contrast to the results of Harris [17].

2.2. *Adaptive Mesh Refinement*

Another major advance of the current model over previous 3D models is the incorporation of an adaptive mesh scheme. As the bubble contracts and more and more elements are being drawn into the developing jet, the aspect ratios of some elements become very large and elements surrounding some nodes become highly nonuniform and irregular. This is of course highly undesirable from a numerical viewpoint and will lead to an early breakdown of computation. The inclusion of an adaptive mesh scheme offers part of the solution to this problem and it prevents the bad aspect ratio and nonuniformity of element sizes from developing. There are many kinds of adaptive schemes. We adopt one in which all the sides of the triangles exceeding twice the average length are halved. Simple test runs indicate that

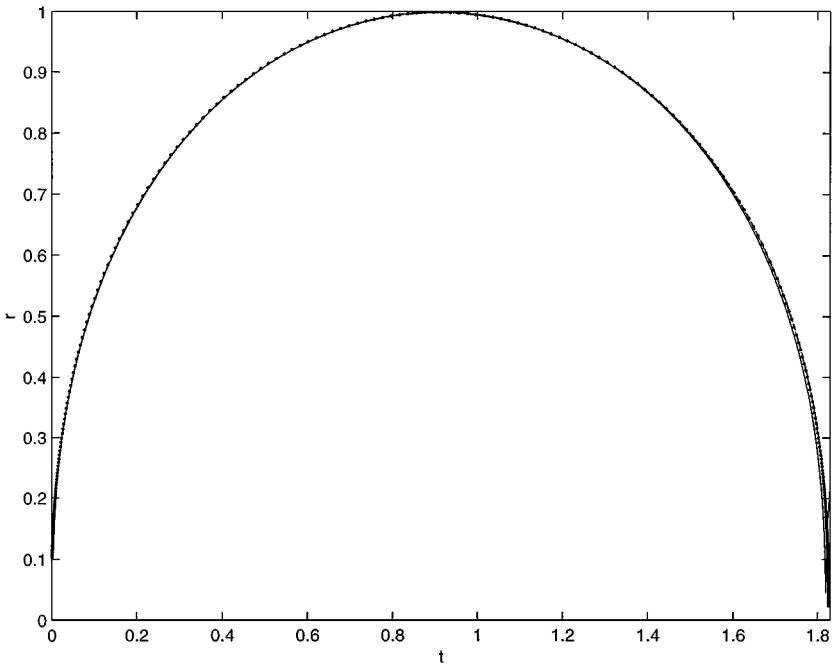

FIG. 2. The time history of the Rayleigh bubble radius calculated from the Rayleigh–Plesset equation using a fourth-order Runge–Kutta method (solid line), the 3D model using the linear averaging method with 162 nodes (dash line), 252 nodes (dots), and 362 nodes (dash-dot line) being used.

this scheme has indeed produced a relatively uniform mesh with a reasonably small aspect ratio in each element. It is also very economical, as an initially coarse mesh can be used with extra nodes being added in the places where the resolution becomes poor. It far outperforms schemes which start with a fine initial mesh but apply no adaptive remeshing. There, a large number of nodes are crammed into the jet with inadequate resolution elsewhere on the bubble and some of the elements in the reentrant jet become highly elongated in the direction of jet advancement.

2.3. *Smoothing Scheme*

The adaptive meshing of the bubble does not prevent severe numerical instability from developing during computation. As can be seen from Figs. 3 and 4a, towards the end of the collapse phase, numerical instability begins to manifest itself as sharp corners and reentrances on the surface of the bubble. If not controlled, these irregularities will amplify rapidly and bring the development of the jet to a halt with their high velocities. Computation then comes to a virtual stop while the jet is still quite far away from the opposite face of the bubble. This is, of course, a purely computational difficulty, since experiments have indicated that the jet will quickly hit the opposite face. The exact causes for these numerical instabilities are not yet fully understood. The recent works of Hou *et al*. [18] and Baker and Nachbin [19] on two-dimensional Hele-Shaw bubbles and vortex sheet motion have shown that the clustering of nodal points may impose a severe limit on the stable time-step size and that this limitation may be somewhat ameliorated by a redistribution of the nodal points. Such redistribution of Lagrangian nodes, based on arc-length spline interpolation, had in fact been employed by Best [8] and Wang *et al*. [6] in their axisymmetric bubble

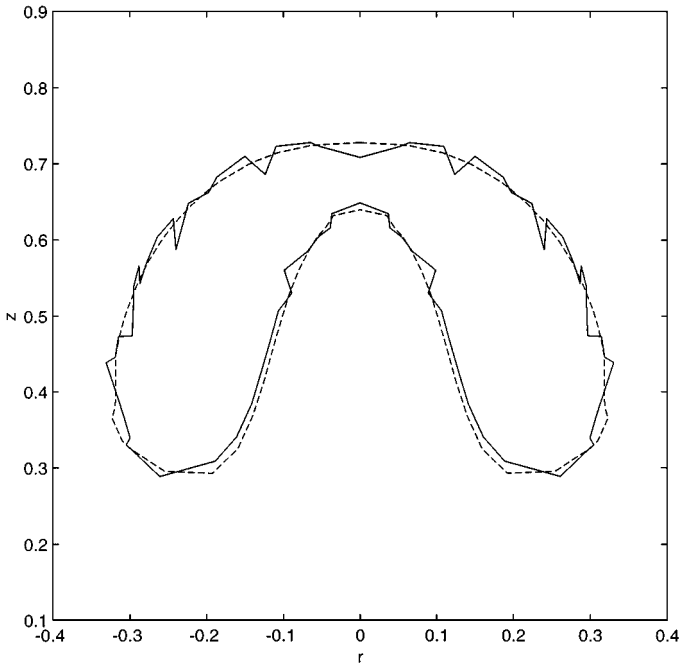

FIG. 3. The bubble profile at $t = 2.1666$, calculated with (dash line) and without (solid line) smoothing. The wall is situated at $z = 1.5$ and $\delta = 0, \epsilon = 100$.

works. Arc-length-based spline interpolation also appears to have some smoothing effects on high-frequency features and errors because of its implicit smoothness. The stability results of Hou *et al*. [18] may also be generically significant to other time-based boundary integral problems. It is not straightforward, however, to extend their analysis to the present 3D problem to determine a rigorous time-marching criterion to replace (7).

The jet impact that arises in the rapid collapse of bubbles is a violent physical event, involving as it does the collision of a fast-moving fluid jet into a slow-moving fluid wall. Despite that, many of the bubbles captured in the experiments had retained a fairly well-defined, and sometime relatively smooth, profile for some time into their toroidal phase [20–22]. This is especially true of bubbles with a narrow liquid jet, where significant surface corrugations occur mainly in the vicinity of the impact point. Cavitation bubbles show greater tendency than gas bubbles to break up at jet impact, partly because the collapse tends to be more violent in the absence of a resisting gaseous medium. For small bubbles, which is the case with the experiments, the effects of viscosity and surface tension are also likely to be more significant and possibly destabilizing to the surface. The present work is more concerned with gas bubbles of a significant size, where the effect of buoyancy is nonnegligible. For these bubbles, the effects of viscosity and surface tension are likely to be much less significant than the effects of inertia. Inertia is the dominant driving mechanism in the evolution of a pulsating bubble and is the mechanism modelled by the present work.

Given the violent nature of the jet impact phenomenon, one can expect any attempt at its simulation to be plagued by strong and persistent instabilities, and the causes of these are not all numerical. The process of jet impact represents a physical singularity in time and space, singular in the sense that it is a discontinuous process in time and space. The transformation to toroidal bubble during jet impact represents no less than a change in the topology of the

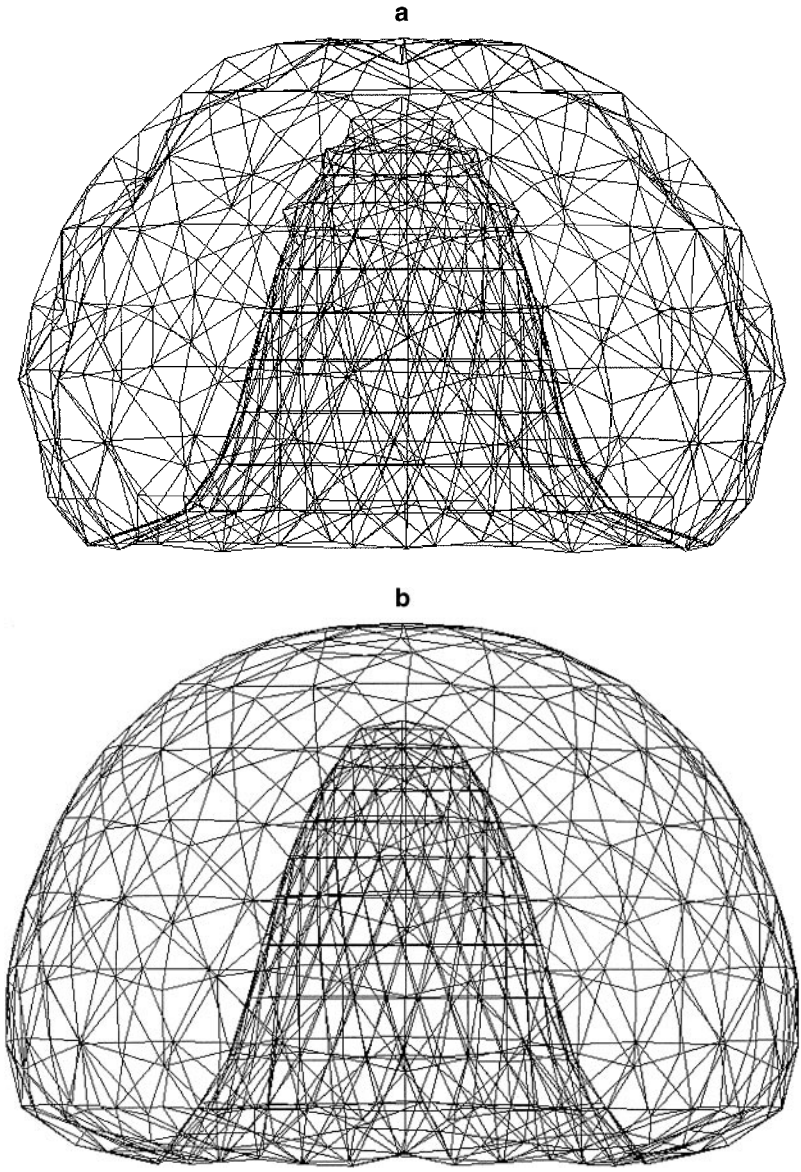

FIG. 4. The 3D view of the bubble, calculated (a) without any smoothing being applied to it, (b) with a smoothing being applied to it, near the end of the collapse phase ($t = 2.1694$ for (a) and $t = 2.1674$ for (b)). The bubble is characterized by the same parameters as in Fig. 3.

underlying fluid domain. In the physical world, this singularity is smeared over time and space by material compressibility and viscosity (and associated turbulent diffussion, etc.). But for simplicity, these physical attributes are not represented in the present mathematical model. A purely inertia model, such as the present, possesses no physical means for smearing the singularity at impact. From a numerical viewpoint, singularity spells trouble. If the singularity is integrable, we can hope to capture its principal properties and effects with a finite-resolution numerical scheme, albeit a rather fine one. In numerical simulation, smearing of singularity occurs naturally as a consequence of the finite discretization of time and space. But this smearing of the singularity is actually an error and does not represent a

physical event. We can keep this error acceptably small, however, by employing a fine mesh and small time steps. Indeed, a fine mesh is necessary to adequately resolve the features near a singularity. In theory at least, singular event requires infinitely fine mesh and time steps to resolve. In the context on the present problem, a relatively fine mesh near the impact point is also essential to keep the errors due to domain surgery small. However, with a fine mesh, the time steps becomes prohibitively small, $O(h^3)$ according to the 2D analysis of Hou *et al*. [18], where h is the smallest mesh size. The smallness of the time step is further greatly aggravated by the very high velocity of the liquid jet (100 to 200 m/s for a relatively small bubble), so that the progress of the simulated event comes almost to a standstill. To move the simulation forward in time, significantly larger time steps are needed. This then leads to high-frequency instability and errors and the collapse of computation. In order to move forward with acceptably larger time steps, it is necessary to *remove* or *filter out* these errors so that they do not grow to jeopardise the computation. The is the role of the smoother.

A concern raised with the use of the smoother is that the fine features produced by the highly singular nature of impact may be lost. This is a genuine concern. However, on further reflection, one will realise that these fine features would in reality interact strongly with viscous and surface tension effects, effects that are after all not incorporated in the model. The fine features therefore represent a higher-order effect, which would be of little significance for a large bubble. Their removal is hence not inconsistent with the neglect of viscosity and surface tension in the model. We therefore believe that the principal dynamics of the bubble and jet impact, with respect to inertia and momentum, will be well captured in spite of smoothing. With a suitable smoother, significantly larger time steps (although still quite small) can be used to move the computation forward.

The 5-point local smoothing formula of Longuet–Higgins and Cokelet [23], coming from their landmark numerical study of breaking waves, has been used extensively in the boundary integral study of axisymmetric bubbles [5–8, 24], and these numerical studies have been successful in reproducing many dynamical features of the immediate postimpact bubbles observed in experiments. The effects of viscosity, surface tension, and compressibility are mostly neglected in these studies. Unfortunately, the 5 point formula cannot be easily generalized to 3D bubbles. Spectral filtering would provide a systematic way to remove high-frequency noise/errors, but again it is difficult to construct such a filter for the present 3D setting. A smoothing scheme for 3D bubbles undergoing jetting and transformation to a toroidal form based on a *least-squares principle* is proposed in this paper. The smoother allows the jet to continually advance to the close proximity of the opposite bubble face (even as the numerical conditioning of the problem becomes progressively ill and the problem itself becomes increasingly singular) and the postimpact toroidal bubble to evolve stably and with good overall conservation of energy. To minimize its effects on the physics, smoothing has been applied sparingly as and when necessary to maintain computational stability.

2.4. *A Least-Squares Smoother*

Curve fitting using least squares is commonly used in the analyses of empirical data, to capture the essential trend, defined by a set of control parameters, in a manner that minimizes the squares of the errors (deviations) as contained in the scatter of the data. To put it another way, subject to the limitations of the control parameters in representing the trend, least-squares procedures are optimal in ensuring the minimal loss of information

from the data source. This feature makes least squares ideal for a smoothing procedure that is aimed at removing high-frequency "noise" present in numerical data. This feature also makes the least-squares error reduction principle a powerful tool in the solution of many numerically posed problems, such as in many finite element implementations.

To implement this scheme, we first identify a surface patch on the bubble comprising a particular node (which will be referred to as node 1), its n immediate neighboring nodes, and the m immediate neighbors of the n nodes. This yields a 2-tier nodal structure around the central node 1 which resembles the 5-point structure used in a typical 5-point smoothing formula, whereby a particular node and two of its adjacent nodes on either side are involved. It also conveniently guarantees that there are always a sufficient number of nodal points for the following least-squares scheme. A local coordinate system $O' - x'y'z'$ is then established on this local surface patch, with the origin being located at node 1 and the z' axis pointing in the direction of the outward normal. With reference to this local frame, the smoothed surface is represented by a biquadratic function,

$$\tilde{z}' = a_1 x'^2 + a_2 x' y' + a_3 y'^2 + a_4 x' + a_5 y' + a_6 \equiv f(x', y'), \tag{10}$$

where the coefficients, a_i $(i = 1, \ldots, 6)$ are found by minimizing the error function,

$$\mathcal{L}(a_1, \ldots, a_6) = \sum_{j=1}^{m+n+1} [f(x'_j, y'_j) - z'_j]^2, \tag{11}$$

where the sum of squres is taken over all the nodal points in the surface patch. After a_i are found, the corrected or smoothed coordinates of the central node 1 are simply $(0, 0, a_6)$. The same procedure is also applied to smooth the potential function ϕ.

There is a problem, however, with regard to the construction of the local frame, since the normal is unknown *a priori*. Here we adopt an iterative scheme, outlined below, that allows the normal and the smoothed surface to be calculated at the same time:

(i) Make an initial guess of the unit normal $\mathbf{n}_0$ at node 1. For this, an averaging scheme such as (9) will do fine.
(ii) Construct a local frame based on $\mathbf{n}_{k-1}$.
(iii) Compute the smoothed surface according to (10) and (11).
(iv) Compute the new normal to the smoothed surface at node 1,

$$\mathbf{n}_k = \pm \frac{(a_4, a_5, -1)}{\sqrt{1 + a_4^2 + a_5^2}}, \tag{12}$$

where the sign can be chosen such that $\mathbf{n}_k \cdot \mathbf{n}_{k-1} > 0$.

(v) If $\|\mathbf{n}_k \times \mathbf{n}_{k-1}\| < \varepsilon$ where ε is a pregiven small constant, the iteration stops; otherwise assign $\mathbf{n}_{k-1} = \mathbf{n}_k$ and go back to (ii), until the result converges.

In our computation, we found that the number of iteration needed is no more than 5 for $\varepsilon = 0.001$ and therefore this part of the computation consumes a minimal amount of CPU time. The above local smoothing procedure is applied to each nodal point on the bubble surface to remove high-frequency local fluctuations. The smoothing does not prevent the bubble surface from developing high-order variations on a global basis, unless those variations approach the fine-scales of the local fluctuations.

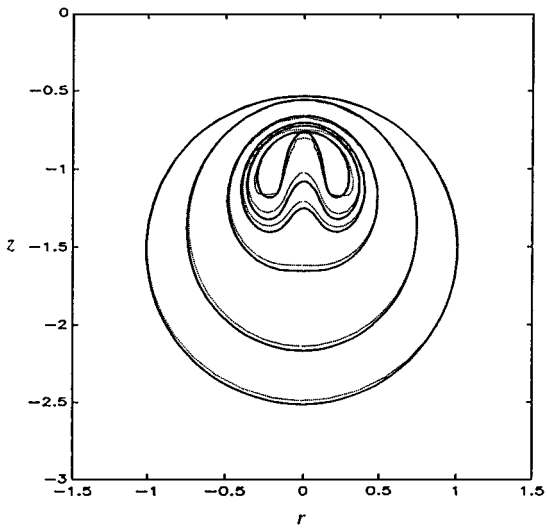

FIG. 5. Comparison of the evolution of the bubble (with the same characteristic parameters as in Fig. 3) during the collapse phase. The timings of successive profiles using the axisymmetric model of Wang *et al*. [b, 30] (full-line) $t = 1.093$ (outermost), 1.842, 2.077, 2.129, 2.148, 2.182 (innermost); using the current 3D model with smoothing and adaptive meshing (dots), $t = 1.093$ (outermost), 1.842, 2.077, 2.129, 2.148, 2.171 (innermost).

The effectiveness of the smoothing can be clearly seen in Figs. 3 and 4. Without any smoothing, the bubble surface wrinkles as the jet forces its way into the interior of the bubble, with zigzags appearing almost everywhere on the bubble surface and the regularity of the surface slowly deteriorating with time (Figs. 3 and 4a). The smoothing scheme, on the other hand, has not only ironed out the wrinkles but also preserved well the surface profile and the forward motion of the bubble jet (Figs. 3 and 4b). As a result, the jet can now advance into striking range of the opposite face of the bubble and be well poised for imminent impact (Fig. 4b).

As a summary, a comparison is made in Fig. 5 between the axisymmetric and 3D results for a bubble undergoing jetting (the *pretoroidal* phase). To minimize the loss of momentum due to smoothing, we have applied the smoothing scheme only sparingly, and not until the liquid jet has advanced to within a very short distance of the opposing bubble wall (typically the last 50 time steps prior to the impact) is the smoothing switched on and applied to the solution every 10 time steps. It can be seen from Fig. 5b that the instability starts to manifest on the 3D bubble surface as it collapses but is eventually eliminated by the smoother. The overall agreement between the two models is very satisfactory. As explained in two of our recent papers [14, 15], the axisymmetric solution tends to evolve slower than the 3D solution. This may be due to the extensive application of smoothing during the whole collapse phase in axisymmetric models to maintain numerical stability. This may be demonstrated with a simple test where the solid wall is placed so far away from the bubble that its influence on the latter is virtually negligible and thus the bubble resembles a Rayleigh bubble (cf. [14]). In this case, the axisymmetric solution evolves slightly slower than the Rayleigh bubble, while the 3D solution is virtually indistinguishable from the latter. The frugal use of smoothing towards the end of the bubble collapse should not significantly alter the accuracy of our results. Another comparison is made in Fig. 6 of the "final" profiles of the bubble computed from the two models just before a surgery is carried out in the impact model (i.e., when the

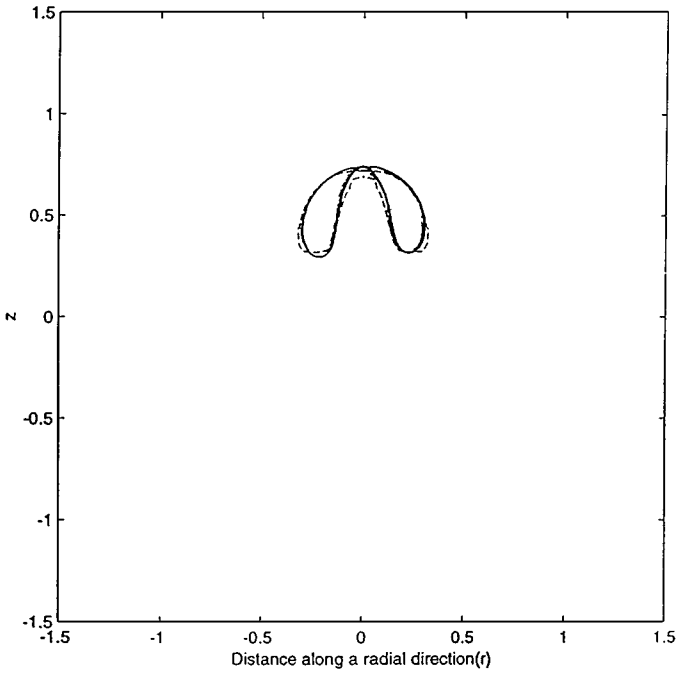

FIG. 6. The bubble profiles just prior to the jet impact, calculated from the axisymmetric model [30] (solid line, with $t = 2.182$) and the 3D model (dash line, with $t = 2.171$).

distance between the north and south poles is less than a certain amount, say 0.03). Again good agreement is observed between the two solutions.

3. JET IMPACT MODEL

3.1. *Surgical Cut*

The fluid domain becomes doubly connected when the liquid jet impacts on the opposite face of the bubble near the end of the collapse phase. This and other forms of interaction among surfaces or fronts in a fluid have posed considerable difficulties to the fluid numericists. There are two basic groups of methods for dealing with such interface problems: front-capturing methods and front-tracking methods. Front-capturing methods do not track the interfaces directly. In particular, a popular front-tracking method, the level-set method (see Sussman *et al*. [25]), is based on the convection of a scalar property defining the interfaces in an Eulerian setting. Complex topological changes of the interfaces are captured in the changing contours of the associated scalar function. Front-capturing procedures tend to be weak for problems that demand a high-order of geometrical accuracy at the interface, such as in problems that are governed by surface tension. For problems with a Lagrangian bias, such as the present, the direct tracking of the interface or front is the more natural scheme—more so, because the boundary integral computation involves only surface quantities. The weaknesses of front tracking procedures are the difficulties of knowing when surfaces come into contact and the need to reconfigure the interacting surfaces in a manner that is consistent with the physics. These are nontrivial tasks. Fortunately, for the jet impact problem considered in this paper, the geometry of the impacting surfaces is fairly simple. A

more thorough review of front-tracking procedures for bubbles and droplets in more general flow settings may be found in Unverdi and Tryggvason [26].

The impact process is physically a very complex one. Here we shall further restrict our study to the idealized case where the impact occurs at a single point, and the effects of the impact are entirely transformed into a circulation in the fluid domain. We also extend Wang *et al.*'s axisymmetric model of jet impact [6] to a 3D setting where the ring is not necessarily planar.

To go into the toroidal phase, a surgical cut must be made to transform the fluid domain Ω from a singly connected to a doubly connected region. To perform the surgical cut, we first identify two nodes, n_0^1 and n_0^2 (one on the advancing jet and the other on the opposite bubble face, respectively), that are nearest to the anticipated point of impact. The two nodes are selected when the jet tip approaches within, say, $0.03R_m$ of the opposite face. Their immediate neigbours, n_i^1 $(i = 1, \ldots, K_1)$ and n_j^2 $(j = 1, \ldots, K_2)$, are also identified. If the numbers of nodes around the two points n_0^1 and n_0^2 do not match (i.e., $K_1 \neq K_2$), additional nodes are inserted along the appropriate line segments to bring the numbers to par. We may hence assume that $K_1 = K_2 \equiv K$. A new set of nodes n_i^3 $(i = 1, \ldots, K)$ is then created at the midpoints

$$\mathbf{x}_{n_i^3} = \left(\mathbf{x}_{n_i^1} + \mathbf{x}_{n_i^2}\right)/2 \tag{13}$$

between the corresponding n_i^1 and n_i^2 nodes. The nodes n_i^1 belonging to the jet and n_i^2 on the opposing wall are then relocated to their midpoint node n_i^3 $(i = 1, \ldots, K)$; and the nodes n_i^1 and n_j^2 $(j = 0, \ldots, K_2)$ are discarded. With this surgery, the two surfaces are now stitched as one along the line segments connecting the n_i^3 nodes, thus forming the eye of the torus. The selection of the two impact nodes n_0^1 and n_0^2 as well as the matching of the nodal pairs n_i^1 and n_i^2 $(i = 1, \ldots, K)$ may be facilitated with a visualization tool such as PATRAN.

3.2. *3D Vortex-Ring Model*

The principal idea of the vortex-ring model is to decompose the total potential ϕ into two parts: a potential associated with the circulation generated by the impact, ψ, termed the ring potential, and a remainder, φ which is smooth in the entire fluid domain,

$$\phi(\mathbf{x}, t) = \psi(\mathbf{x}) + \varphi(\mathbf{x}, t). \tag{14}$$

The circulation of the flow Γ around the vortex tube is modelled by placing a vortex ring within the *interior* of the vortex tube. The velocity potential ψ generated by this ring vortex is a multivalued function. A single-valued branch of ψ may be selected by introducing an imaginary surface S_c stretching over the ring, across which the potential ψ jumps by an amount Γ equal to the strength of the vortex ring. This imaginary surface of discontinuity S_c may be made to coincide with the impact surface, but this is not a necessary condition.

To construct the vortex ring, we construct a set of nodes, n_i^4 $(i = 1, \ldots, K)$. These are placed at a small distance from the corresponding nodes n_i^3 along the outward normal direction (into the bubble). The vortex ring is then assumed to thread sequentially through the vortex tube along the nodal loop formed sequentially by the n_i^4 $(i = 1, \ldots, K)$ in a piecewise-linear fashion. The exact placement of the ring is immaterial from a theoretical viewpoint so long as the ring is completely inside the torus. This is because any change

in the vortex-induced potential ψ due to its placement would be exactly compensated for in the remaining part φ according to (14). Note that the piecewise-linear vortex ring in the general 3D case is no longer planar. The strength of the vortex ring Γ should reflect the jump in potential across the contacting points during the impact process:

$$\Gamma = \phi_{n_0^1} - \phi_{n_0^2}. \tag{15}$$

The velocity field of the vortex ring $\mathbf{v}_R$ may be computed directly from the Biot–Savart law,

$$\mathbf{v}_R(\mathbf{x}, t) = \frac{\Gamma}{4\pi} \sum_{j=1}^{K} \int_{n_j^4}^{n_{j+1}^4} \frac{\mathbf{r}(\mathbf{x}, \mathbf{x}') \times d\mathbf{l}(\mathbf{x}')}{r^3}, \tag{16}$$

where $n_{K+1}^4 \equiv n_1^4$, $\mathbf{r}(\mathbf{x}, \mathbf{x}')$ is a vector from a source point $\mathbf{x}'$ on the ring to a field point $\mathbf{x}$ being considered, and $r = \|\mathbf{r}\|$. The ring potential ψ for any point in the flow field may then be obtained by integrating the velocity field from a suitable reference point along a path that avoids the surface of discontinuity S_c. This course was adopted in our earlier axisymmetric work [1] and the earlier version of the three-dimensional work. Employing a result from Milne–Thomson [27], the ring potential at any point $\mathbf{x}$ in the flow field or the bubble surface can be more efficiently obtained by

$$\psi(\mathbf{x}) = \frac{\Gamma \Theta(\mathbf{x})}{4\pi}, \tag{17}$$

where

$$\Theta(\mathbf{x}) = \int_{S_c} \frac{\partial}{\partial n} \left(\frac{1}{r} \right) dS \tag{18}$$

is the *solid angle* subtend at the point $\mathbf{x}$ by the surface of discontinuity S_c that extends over the vortex ring. Applying a simple triangulation to S_c, $\Theta(\mathbf{x})$ is then equal to the arithmetic sum of the solid angles subtended by the triangles of S_c at $\mathbf{x}$, with the sign of the angles being taken in accordance with the normal on S_c. The sense of the normal on S_c is governed by the sign of Γ following the usual right-hand screw rule. The computation of $\psi(\mathbf{x})$ is thus reduced to one of calculating the solid angles of spherical triangles for which standard formula is available; see [28]. $\Theta(\mathbf{x})$ suffers a jump of 4π across S_c so that the ring potential ψ jumps by an amount equal to Γ. It can be seen from (17) that $\psi \to 0$ as $\mathbf{x} \to \infty$.

We note that ψ satisfies the boundary integral equation (3) because it is a solution of the Laplace equation in the fluid domain and tends to zero at infinity. The remainder potential φ should thus also satisfy the same boundary integral equation and farfield boundary condition. φ is smooth because the jump in the total potential ϕ due to flow circulation is captured in ψ. With the ring potential ψ having been prescribed, the evolution of the toroidal bubble is now governed by the remainder potential φ. The boundary conditions on the bubble surface S_b(5) must now be modified for use with φ. They are

$$\frac{D\mathbf{x}}{Dt} = \nabla\varphi + \mathbf{v}_R, \tag{19}$$

$$\frac{D\varphi}{Dt} = -\mathbf{v}_R \cdot (\mathbf{v}_R + \nabla\varphi) + 1 + \frac{1}{2}\|\nabla\varphi + \mathbf{v}_R\|^2 - \delta^2 z - \epsilon \left(\frac{V_0}{V} \right)^{\lambda}, \tag{20}$$

where $\mathbf{v}_R$ is the velocity field produced by the ring vortex, which may be computed from (16) or the direct differentiation of ψ. The solution of the boundary integral equation for φ and its marching in time follow that of ϕ as described in Section 2.1.

The evolution of the immediate postimpact bubble is plagued by strong instabilities, which may be both numerical and physical. These violent instabilities are kept in check by the smoothing scheme which is applied to φ every 10 time steps after the impact. Adaptive mesh refinement is implemented throughout the toroidal phase as well, and as a result, the vortex ring is also refined. In addition, one must also update the position of the vortex ring along with the changing shape of the toroidal bubble to ensure that the ring stays well within the bubble.

The typical computation in a time step involves the following: (i) compute the distribution of ψ on the bubble given the current position of the vortex ring, (ii) compute φ on the bubble using (14), (iii) solve the boundary integral equations (3), and (8) to determine $\nabla\varphi$, (iv) integrate (19) and (20) to find the new bubble surface and the new distribution of φ on it, (v) compute the total potential ϕ at the new bubble surface using (14), (vi) apply smoothing as necessary, (vii) introduce a new vortex ring as necessary, and (viii) repeat from step (i) for the next time step.

4. REBOUNDING OF THE TOROIDAL BUBBLE

As observed in the axisymmetrie case, the bubble will continue to shrink for a short while after its transition to toroidal form before it rebounds. The high pressure inside the bubble near its minimum volume was believed to cause another pressure peak and be responsible for the "slamming" effect on nearby solid boundary [29].

Figures 7 and 8 show two series of bubble profiles produced from the new 3D model and the axisymmetric model of Wang *et al*. [6, 30]. A shift in the z coordinates has been made in our results to accommodate the different location of the coordinate origin adopted in [30]. A major difference between the two is the duration of the toroidal phase; our results indicate a far smaller lifetime for the toroidal bubble before it "reconnects" itself to become singly connected again [8]. Also some of the detailed features on the axisymmetric bubble (a more corrugated surface) are absent in the 3D results. This could be due to the more limited resolution in 3D cases. Furthermore, the circulation caused by the impact and the rotation of the toroidal bubble are more obvious in the 3D results. With no experimental data available, it is difficult to judge which model is more accurate. However, the essential physics associated with a jet impact, such as the circulation and rebounding, is successfully captured in the new model.

The most important application of the 3D model lie of course in situations where the assumption of axisymmetry ceases to be valid. One such situation concerns the collapse of buoyant bubbles in the vicinity of a vertical wall situated at $x = 1.5$, for which two sets of results are presented below. Buoyancy causes a collapsing bubble to develop a jet that shoots upwards, whereas the Bjerknes force causes a similar jet to be directed towards the wall. The combined effect hence induces an oblique jet whose angle of inclination is determined by the relative strength of the two forces. A low buoyancy case, $\delta = 0.05$, is shown in Figs. 9 and 10. These give the postimpact views of the bubble from two angles; Fig. 10 gives the side views of the bubbles in Fig. 9. Figures 9a and 10a show two views of the bubble just after jet impact. The bubble continues to shrink in its postimpact phase to its

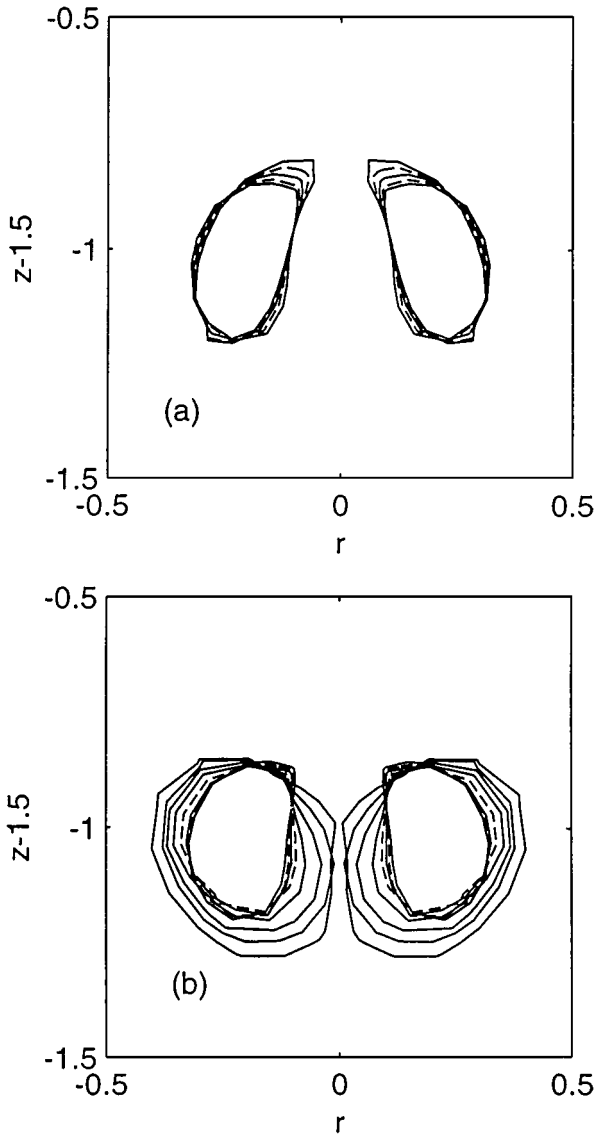

FIG. 7. Evolution of toroidal bubble predicted by the current 3D model. Continued from the 3D results of Fig. 5, (a) collapse phase at $t - t_0 = 0$ (outermost), 7.4×10^{-4}, 1.22×10^{-3}, 1.51×10^{-3}, 1.56×10^{-3} (innermost), and (b) rebounding phase at $t - t_0 = 1.56 \times 10^{-3}$ (innermost), 1.59×10^{-3}, 1.61×10^{-3}, 1.66×10^{-3}, 1.70×10^{-3}, 1.71×10^{-3}, 1.73×10^{-3}, 1.75×10^{-3}. The circulation is $\Gamma = 4.56$ and the impact time is $t_0 = 2.17147$.

minimum volume in view (c), after which it rebounds almost radially with a slight elongation along the direction of buoyancy. The jet is inclined at a fairly small angle to the horizontal (due to the weak buoyancy effect), with a larger volume of gas below the jet axis (Figs. 10a–10d). The jet remains intact during much of this collapsing phase but is strongly squeezed to a thin tube as the bubble rebounds (Figs. 10d and 10e), suggesting that the axial momentum of the jet has become greatly reduced during this phase of bubble development. *Reconnection* of bubble surface, which will return the now toroidal bubble to its original simply connected geometry, is expected to occur near the mid section of the jet shortly thereafter. Typically, the

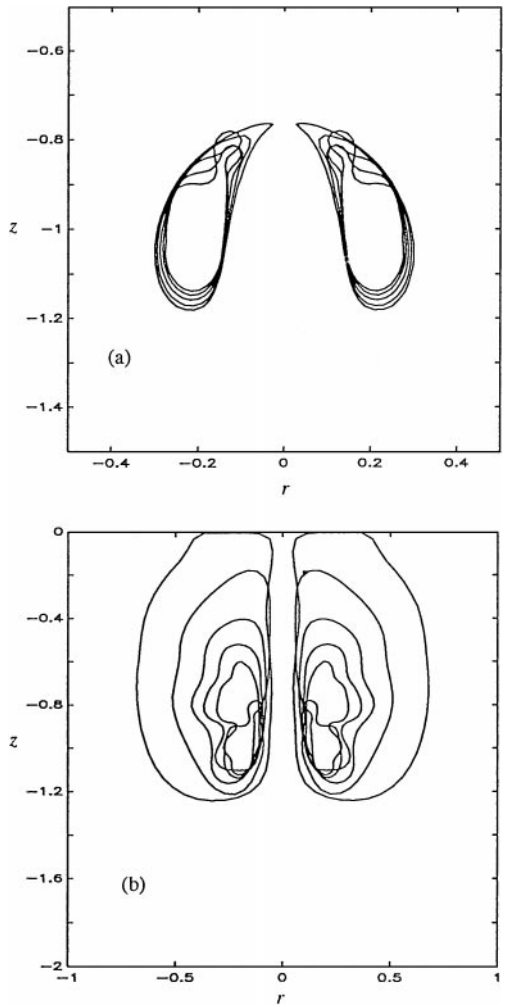

FIG. 8. Evolution of toroidal bubble predicted using the axisymmetric model [30]. Continued from the axisymmetric results of Fig. 5, (a) collapse phase at $t = 2.1823$ (outermost), 2.1852, 2.1895, 2.1978 (innermost), and (b) rebounding phase at $t = 2.1978$ (innermost), 2.2199, 2.2322, 2.2519, 2.2807, 2.3446, 2.4961 (outermost). The circulation is $\Gamma = 4.72$.

numerical problem becomes ill-conditioned, tending towards singularity, as reconnection is approached. However, we do not expect the problem to be as severe as the jet impact case where one surface approaches another at great speed, and damping or smoothing is required to control the strong (physical and numerical) instabilities that accompany the impact. Modelling of the reconnection, which will require further geometrical reconstruction of the contacting surfaces, is not attempted here. Despite the violence of the impact, the solution has remained highly symmetrical with respect to the y axis in Fig. 9, indicating that the numerical treatment we have applied, including the adaptive mesh refinement, is stable. It can be seen in Figs. 10a to 10c that sharp edges thrown up by the instabilities are kept in check by the smoothing operation.

The scene remains essentially the same for all weak and moderate buoyancy cases, but becomes quite different when buoyancy effect is strong. The postimpact evolution for the

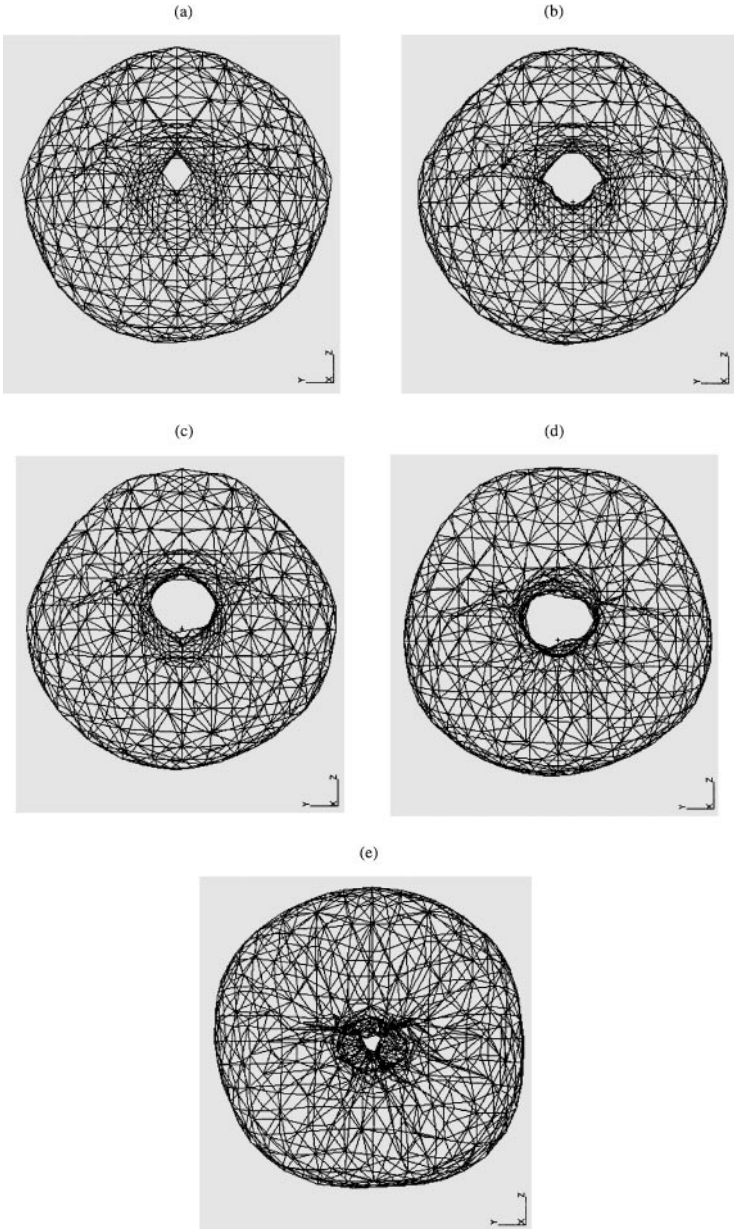

FIG. 9. Evolution of a toroidal bubble, characterized by $\delta = 0.05$ and $\epsilon = 100$, during the collapse phase (a) $t - t_0 = 0$, (b) $t - t_0 = 8.6 \times 10^{-5}$, (c) $t - t_0 = 1.56 \times 10^{-4}$, and rebounding phase (c) $t - t_0 = 1.56 \times 10^{-4}$, (d) $t - t_0 = 1.89 \times 10^{-4}$, (e) $t - t_0 = 2.29 \times 10^{-4}$, with $t_0 = 2.190120$.

case of a buoyant bubble with $\delta = 0.12$ is depicted in Figs. 11 and 12. In this case, the strong buoyancy vehemently drives the jet at a sharp upward angle towards the upper part of the toroidal bubble, squeezing the gas from the upper reaches of the bubble even as it rebounds (Figs. 12c to 12e). The increase in the volume of the bubble during the rebounding phase is thus derived from those parts below the jet. The approaching reconnection between the upper surface of the jet and the top of the bubble leads to severe numerical ill-conditioning and instability that show up as two small horns at the top of the bubble in Fig. 12e. Again

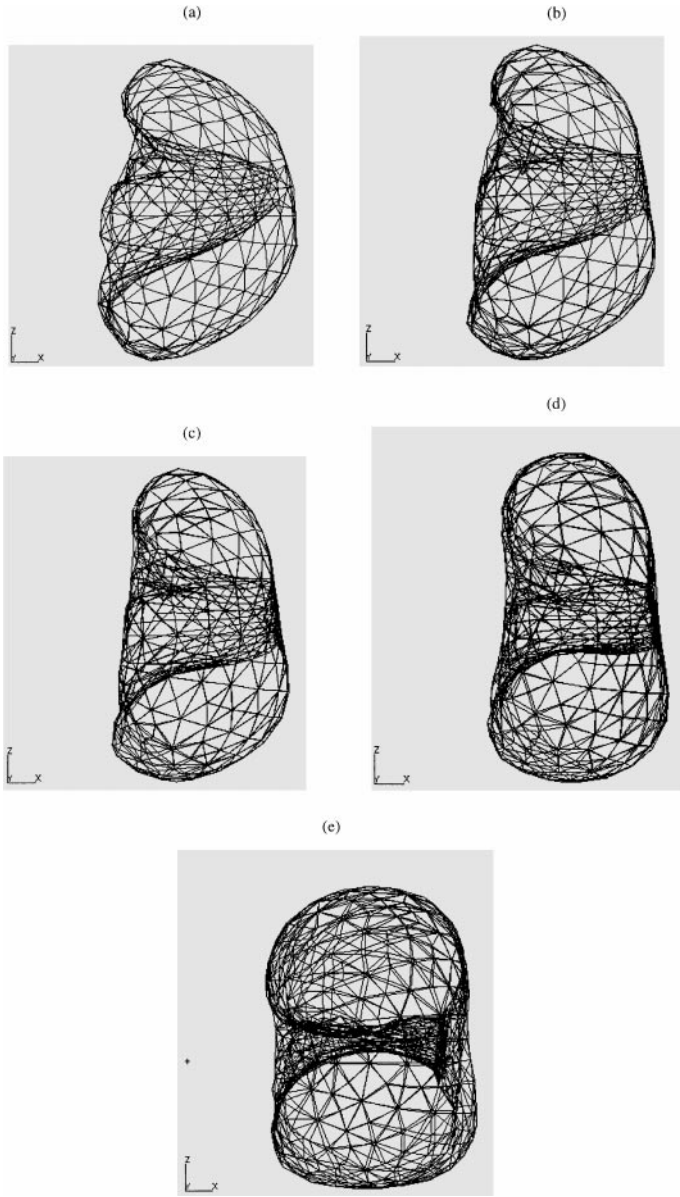

FIG. 10. Evolution of the same toroidal bubble as in Fig. 9, shown here from a different perspective.

the symmetry of the solution is very good in Fig. 11 until the approach of reconnection in Fig. 11e, where a trace of asymmetry becomes visible at the top of the bubble.

The nondimensional total energy of the fluid domain and the bubble content is given up to a constant by

$$\frac{1}{2}\int_{S_b}\phi\frac{\partial\phi}{\partial n}dS+\frac{1}{2}\Gamma Q+V(1-\delta^2 z_c)+\frac{\epsilon V}{\lambda-1}\left(\frac{V_0}{V}\right)^{\lambda}, \tag{21}$$

where the first and second terms represent the kinetic energy of the fluid domain. The second term gives the energy associated with the circulation of flow around the toroidal tube, Q

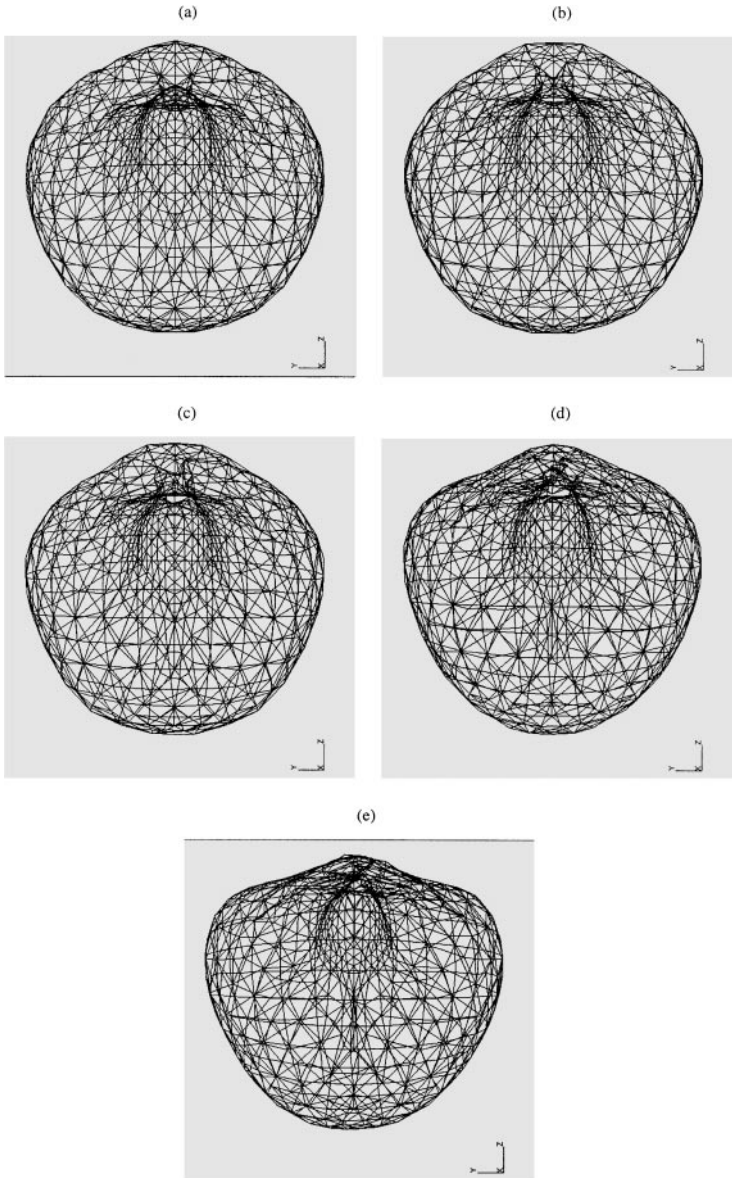

FIG. 11. Evolution of a torodial bubble, characterized by $\delta = 0.12$ and $\epsilon = 100$, during the collapse phase (a) $t - t_0 = 0$, (b) $t - t_0 = 7.4 \times 10^{-5}$, (c) $t - t_0 = 1.07 \times 10^{-4}$, and rebounding phase (c) $t - t_0 = 1.07 \times 10^{-4}$, (d) $t - t_0 = 2.29 \times 10^{-4}$, (e) $t - t_0 = 3.36 \times 10^{-4}$, with $t_0 = 2.184062$.

being the volume flow rate through the eye of the torus. The third term is the potential energy of the fluid domain due to the size and position of the bubble, z_c being the z coordinate of the bubble's centroid. The last term is the potential energy of the bubble content. Energy is conserved in the present one-point jet impact model. In a zone-impact model such as [9], energy may be lost in the impacting process. The loss appears to be very small, however, amounting to about 2% for gas bubbles [31].

Figure 13 shows the fluctuations of the total energy of a collapsing bubble undergoing transition to toroidal geometry. It pertains to the case of a bubble undergoing 3D collapse

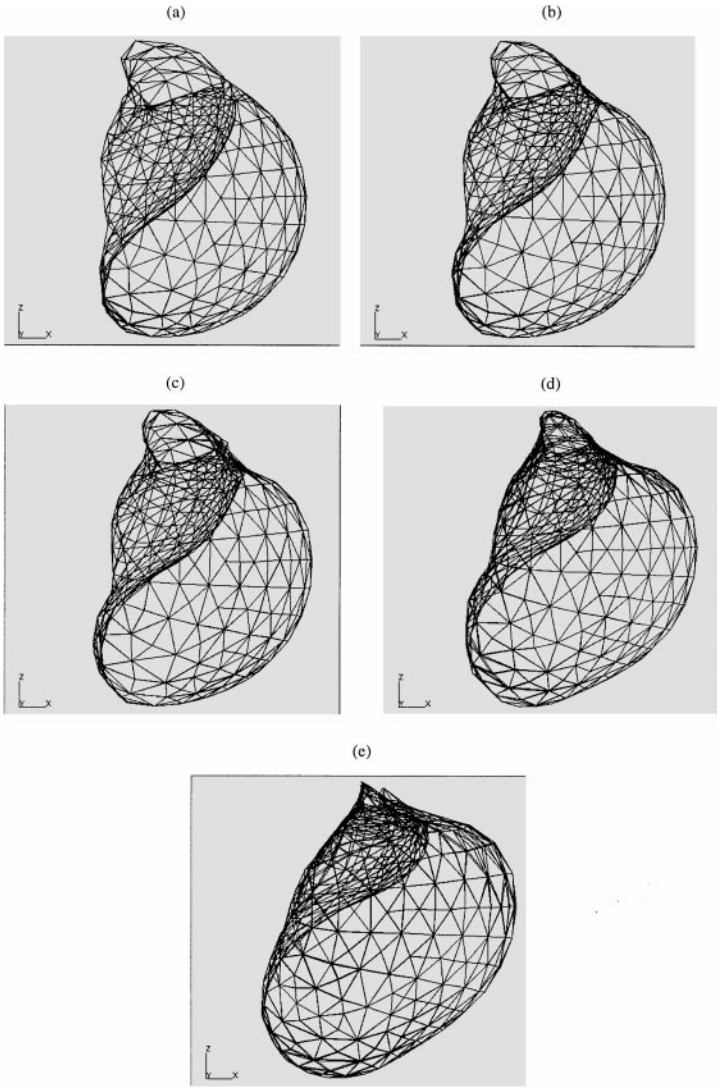

FIG. 12. Evolution of the same toroidal bubble as in Fig. 11, shown here from a different perspective.

and jetting near a spherical-capped cylinder and the jet impact occurred at $t = 1.978$. The least-squares smoother was applied once every 10 time steps in Fig. 13a. In Fig 13b, the smoother was applied once every 10 time steps before the impact and once every three time steps after the impact. Common to both figures was the very sharp fluctuations of energy at the time of jet impact. These fluctuations are due to the strong instabilities associated with the highly singular nature of the jet impact phenomenon, as was discussed in Section 2.3. The fluctuations of the total energy, larger in case (a) than in case (b), fade away with the further evolution of the bubble in its toroidal state. The total energy recovers to within 2% of its steady preimpact level, showing good overall conservation of energy through the impact. The large fluctuations of energy of the immediate postimpact bubble may be attributed to the highly jagged surface of the bubble during this period. The smoother was thus effective in preventing the uncontrolled developments of thse instabilities from putting an abrupt end to the simulation. The open circles in the figures indicate where the smoother had been

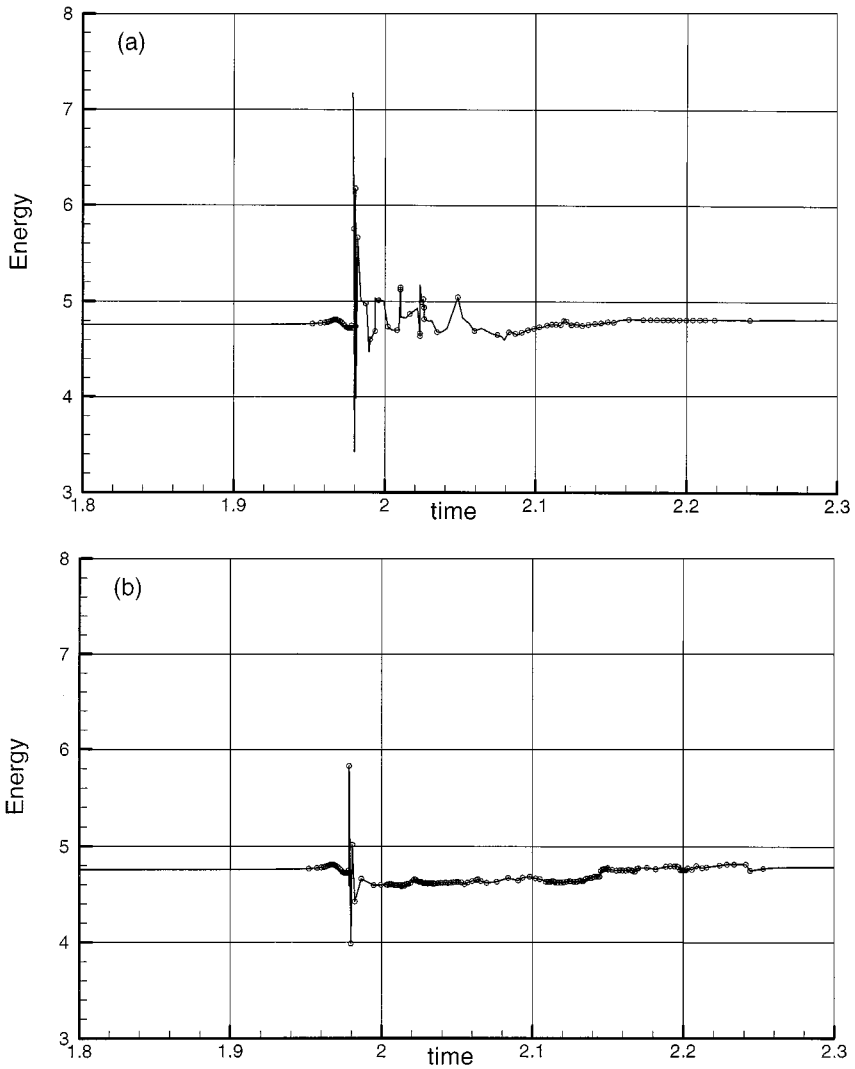

FIG. 13. Time history of variation of total energy through jet impact. The bubble, with $\epsilon = 100$ and $\delta = 0$, was initiated at a distance of 1.5 from the side of a spherical-capped cylinder (diameter 1.0 and overall length 4.0) at 0.5 off mid-cylinderical section. Jet impact time at $t_0 = 1.978417$. The smoother was applied once every 10 time steps in (a) and applied once every 3 time steps after jet impact in (b). Total energy associated with smoothed data is denoted by (○).

applied. Comparing the two cases, the more frequent smoothing applied in (b) was found to result in only a marginal slow down in the development of the posttoroidal bubble. It is also worth noting that the effect of smoothing on the energy is highly stable once initial phase of wild fluctuations is past. This shows that the smoother is fairly energy neutral and does not cause persistent monotonic increase or decrease of energy. Indeed, the smoother has only a very small effect on the energy when the bubble surface is smooth. This is as it should be, since there is then no high-frequency noise or errors that need removing, and the surface should then be left intact by the smoother. This is evident in the steady energy level in the latter part of the toroidal phase in Fig. 13, where we expect the bubble surface to be smooth. The total energy stays constant after smoothing was discontinued. The hump in the

total energy before the impact is due to the instability that sets in as the jet approaches the opposing bubble wall.

We have chosen to focus our attention on key numerical issues in this paper and have thus restricted the theoretical formulation here to cases of 3D bubble interaction with a plane vertical wall. It suffices to note that the extension to general 3D solid structures may be straightforwardly achieved, by modifying Green's function and implementing the necessary normal-velocity boundary conditions for solid surfaces in the boundary integral equation.

5. CONCLUDING REMARKS

A number of new techniques/schemes have been devised to address the numerical problems associated with the simulation of the three-dimensional jetting of bubbles and the ensuing jet impact. These may be summarized as follows:

(i) A weighted-average scheme is used to calculate the material velocity on the bubble surface which guarantees the convergence of the solution.

(ii) An adaptive mesh refinement scheme is introduced to maintain a high degree of mesh regularity and uniformity during the development of the liquid jet. A highly distorted mesh would bring the development of the jet to a premature halt.

(iii) A smoother based on the least-squares principle is encapsulated in the code to keep in check the severe numerical instability that occurs before and after jet impact; it is found to have good energy conservation property.

(iv) A 3D vortex ring is used to represent the circulation of the flow resulting from jet impact and to facilitate the computation of the flow in the postimpact toroidal phase.

Satisfactory results have been obtained with the new 3D bubble model despite some differences being observed between the 3D and axisymmetric impact results. The 3D model and results presented in this paper concern primarily the interaction of bubbles with a plane vertical wall. They serve as a window to an appreciation of the phenomenon of 3D jet impact. Much more can be learned with the new 3D model in the case of the interaction of bubbles with a general solid structure and/or with a free surface, but this is out of the scope of the present paper.

REFERENCES

1. M. S. Plesset and A. Prosperetti, Bubble dynamics and cavitation, *Annu. Rev. Fluid Mech.* **9**, 145 (1977).
2. J. R. Blake and D. C. Gibson, Cavitation bubbles near boundaries, *Annu. Rev. Fluid Mech.* **19**, 99 (1987).
3. J. R. Blake, M. C. Hooton, P. B. Robinson, and R. P. Tong, Collapsing cavities, toroidal bubbles and jet impact, *Phil. Trans. R. Soc. Lond. A* **355**, 537 (1997).
4. L. Guerri, G. Lucca, and A. Prosperetti, A numerical method for the dynamics of non-spherical cavitation bubbles, in *Proc. 2nd Int. Colloq. on Drops and Bubbles* (California, 1981), p. 175.
5. J. R. Blake, B. B. Taib, and G. Doherty, Transient cavities near boundaries. 1. Rigid boundary, *J. Fluid Mech.* **170**, 479 (1986)
6. Q. X. Wang, K. S. Yeo, B. C. Khoo, and K. Y. Lam, Nonlinear interaction between gas bubble and free surface, *Comput. Fluids* **25**, 607 (1996).
7. J. P. Best, *The Dynamics of Underwater Explosions*, Ph.D. thesis (Univ. of Wollongong, Australia, 1991).
8. J. P. Best, The formation of toroidal bubbles upon collapse of transient cavities, *J. Fluid Mech.* **251**, 79 (1993).
9. S. Zhang, J. H. Duncan, and G. L. Chahine, The final stage of the collapse of a cavitation bubble near a rigid wall, *J. Fluid Mech.* **257**, 147 (1993).

10. T. S. Lundgren and N. N. Mansour, Vortex ring bubbles, *J. Fluid Mech*. **224**, 177 (1991).
11. S. A. Wilkerson, *A Boundary Integral Approach to Three Dimensional Underwater Explosion Bubble Dynamics*, Ph.D. dissertation (Johns Hopkins University, Baltimore, MD, 1990).
12. G. L. Chahine, Numerical modelling of dynamic behavior of bubble in nonuniform flow fields, in *ASME Symposium on Numerical Method for Multiphase Flows* (Toronto, 1990).
13. R. P. Tong, A new approach to modelling an unsteady free surface in boundary integral methods with application to bubble–structure interactions, *Math. Comput. Simulation* **44**, 415 (1997).
14. Y. L. Zhang, K. S. Yeo, B. C. Khoo, and W. K. Chong, Three-dimensional computation of bubbles near a free surface. *J. Comput. Phys*. **146**, 105 (1998).
15. Y. L. Zhang, K. S. Yeo, B. C. Khoo, and W. K. Chong, Simulation of three-dimensional bubbles using desingularized boundary integral method, *Int. J. Num. Methods. Fluids* **31**, 1311 (1999).
16. J. R. Blake, J. M. Boulton-Stone, and R. P. Tong, Boundary integral methods for rising, bursting and collapsing bubbles, in *BE Applications in Fluid Mechanics*, Vol. 4, edited by H. Power, Computational Mechanics Publications, Southampton, U.K. (1995), p. 31.
17. P. J. Harris, A numerical model for determining the motion of a bubble close to a fixed rigid structure in a fluid, *Int. J. Num. Methods Eng*. **33**, 1813 (1992).
18. T. Y. Hou, J. S. Lowengrub, and M. J. Shelley, Removing the stiffness from interfacial flows with surface tension. *J. Comput. Phys*. **114**, 312 (1994).
19. G. Baker and A. Nachbin, Stable methods for vortex sheet motion in the presence of surface tension, *SIAM J. Sci. Comput*. **19**, 1737 (1998).
20. Y. Tomita and A. Shima, Mechanisms of impulsive pressure generation and damage pit formation by bubble collapse. *J. Flluid Mech*. **169**, 535 (1986).
21. A. Philipp and W. Lauterborn, Cavitation erosion by single laser-produced bubbles. *J. Fluid Mech*. **361**, 75 (1998).
22. C. D. Ohl, T. Kurz, R. Geisler, O. Lindau, and W. Lauterborn, Bubble dynamics, shock waves and sonoluminescence. *Phil. Trans. R. Soc. Lond. A* **357**, 269 (1999).
23. M. S. Longuet-Higgins and E. D. Cokelet, The deformation of steeps surface waves on water. I. A. numerical method of computation, *Proc. Roy. Soc. Lond. A* **350**, 1 (1976).
24. J. R. Blake, G. S. Keen, R. P. Tong, and M. Wilson, Acoustic cavitation: fluid dynamics of non-spherical bubbles. *Phil. Trans. R. Soc. Lond. A* **357**, 251 (1999).
25. M. Sussman, A. S. Almgren, J. B. Bell, P. Collela, L. H. Howell, and M. L. Welcome, An adaptive level set approach for incompressible two-phase flows. *J. Comput. Phys*. **148**, 81 (1999).
26. S. O. Unverdi and G. Tryggvason, A Front-tracking method for viscous, incompressible multi-fluid flows, *J. Comput. Phys*. **100**, 25 (1992).
27. L. M. Milne-Thomson, *Theoretical Hydrodynamics*, 5th ed. (Dover Publications, New York 1968).
28. L. Rade and B. Westergren, *Mathematic Handbook for Science and Engineering*, 4th Ed. (Springer, 1998).
29. R. P. Tong, W. P. Schiffers, S. J. Shaw, J. R. Blake, and D. C. Emmony, The role of "Splashing" in the collapse of a laser-generated cavity near a rigid boundary. *J. Fluid Mech*. **380**, 339 (1999).
30. Q. X. Wang, K. S. Yeo, B. C. Khoo, and K. Y. Lam, Toroidal bubbles near a rigid wall, Unpublished Technical Report (1996).
31. C. D. Milligan, J. H. Duncan, and S. Zhang, Numerical simulations of experiments of the interaction of a cavitation bubble and a compliant wall, in *Proceedings of FED-Vol 153, Cavitation and Multi-phase Flow, ASME*, 143 (1993).